Materials Today Bio 29 (2024) 101293

Contents lists available at ScienceDirect

Materials Today Bio

journal homepage: www.journals.elsevier.com/materials-today-bio

Biomimetic composite gelatin methacryloyl hydrogels for improving survival and osteogenesis of human adipose-derived stem cells in 3D microenvironment

Eunhyung Kim [a,b,1], Jinkyu Lee [a,1], Se-Jeong Kim [a], Eun Mi Kim [a], Hayeon Byun [a], Seung Jae Huh [a,b], Eunjin Lee [a,b], Heungsoo Shin [a,b,c,*]

[a] Department of Bioengineering, Hanyang University, 222 Wangsimni-ro, Seongdong-gu, Seoul 04763, Republic of Korea
[b] BK21 FOUR, Education and Research Group for Biopharmaceutical Innovation Leader, Hanyang University, Seoul, 04763, Republic of Korea
[c] Institute of Nano Science and Technology, Hanyang University, Seoul, 04763, Republic of Korea

ARTICLE INFO

Keywords:
Hydrogel
Nanoparticle
Radical scavenging
Osteogenesis

ABSTRACT

Gelatin methacryloyl (GelMA) hydrogels are used for stem cell encapsulation in bone tissue engineering due to their fast and stable photo-crosslinking. However, cell viability and ability to induce osteogenesis are reduced by reactive oxygen species (ROS) produced during the crosslinking reaction. In this study, we developed biomimetic nanoparticles (TMNs) by combining tannic acid (TA) and simulated body fluid (SBF) minerals, and used them to synthesize GelMA-based composite hydrogels for addressing those limitations. The optimal concentrations of TA and SBF were investigated to create nanoparticles that can effectively scavenge ROS and induce osteogenesis. The incorporation of TMNs into composite hydrogels (G-TMN) significantly enhanced the survival and proliferation of encapsulated human adipose-derived stem cells (hADSCs) by providing resistance to oxidative conditions. In addition, the ions that were released, such as Ca^{2+} and PO_4^{3-}, stimulated stem cell differentiation into bone cells. The hADSCs encapsulated in G-TMN had 2.0 ± 0.8-fold greater viability and 1.3 ± 1.8 times greater calcium deposition than those encapsulated in the hydrogel without nanoparticles. Furthermore, the *in vivo* transplantation of G-TMN into a subcutaneous mouse model demonstrated the rapid degradation of the gel-network while retaining the osteoinductive particles and cells in the transplanted area. The increased cellular activity observed in our multifunctional composite hydrogel can serve as a foundation for novel and effective therapies for bone deformities.

1. Introduction

Bone tissue engineering uses a combination of cells, bioactive molecules, and scaffolds to replicate the function and structure of natural bone to regenerate large bone defects [1]. Stem cells have commonly been used for this application due to their potential to differentiate into bone-forming cells [2]. The encapsulation of stem cells within a biocompatible hydrogel creates an *in vivo*-like 3-dimensional (3D) microenvironment that is similar to that of natural bone tissue. Such an environment allows interactions between cells and the surrounding matrix, which promotes the growth and metabolic activity of stem cells [3–5]. Gelatin methacryloyl (GelMA) hydrogels are highly suited for this strategy due to their convenient encapsulation of cells and various signaling molecules, rapid crosslinking, and adjustable mechanical strength achieved through reversible thermal and UV-based gelation [6,7]. Nonetheless, GelMA hydrogels containing stem cells have exhibited restricted bone regeneration because of inadequate stimulation of the encapsulated stem cells [8–10]. Thus, it is necessary to create composite system within GelMA hydrogels that can both contain stem cells and effective biomolecules stimulating bone formation to achieve satisfactory multifunctionality.

Hydrogels that contain osteoinductive nanoparticles, such as calcium phosphate–based mineral particles, bioactive glass, or carbon nanotubes (CNTs), have been engineered to induce osteogenic differentiation of stem cells [10–13]. Incorporating hydroxyapatite, SiO_2, or CNT particles in GelMA hydrogels enhanced alkaline phosphatase (ALP) activity,

* Corresponding author. Department of Bioengineering, Hanyang University, Seoul, 04763, Republic of Korea.
E-mail address: hshin@hanyang.ac.kr (H. Shin).
[1] These authors contributed equally to this work.

https://doi.org/10.1016/j.mtbio.2024.101293
Received 25 May 2024; Received in revised form 20 September 2024; Accepted 6 October 2024
Available online 9 October 2024

osteogenic differentiation of encapsulated stem cells, and mineral deposition in a consistent manner [13–16]. Simulated body fluid (SBF) was used to develop a crystalline structure of particles that closely resembled that of the apatite found in natural bone. This crystalline structure, composed primarily of calcium phosphate, facilitated bone regeneration by effectively inducing stem cell adhesion, migration, proliferation, and osteogenic differentiation [17,18]. In bone tissue engineering, SBF has generally been applied as a nanoparticle coating on the surface of bone implants [19,20]. Incorporating SBF-based mineral nanoparticles in GelMA hydrogels might have the potential to induce osteogenic differentiation of encapsulated stem cells and bone regeneration, but the widespread application of GelMA in cell encapsulation has been impeded by the intrinsic chemical process of gelation. The photo-crosslinking of GelMA generally produces reactive oxygen species (ROS) such as H_2O_2, ·OH, and $O_2^{\cdot-}$ that have adverse effects on cells and tissues, including severe inflammation, compromised cell viability, and tissue regeneration setbacks [21].

Polyphenols such as epicatechin gallate, epigallocatechin gallate (EGCG), and tannic acid (TA) have multiple phenolic groups and strong anti-oxidative, anti-bacterial, and anti-inflammatory properties [18,19]. When they are used for tissue engineering, polyphenols are generally coated onto polymeric scaffolds or used to prepare nanoparticles by exploiting their capacity for supramolecular self-assembly through the formation of a metal-phenolic network (MPN) that coordinates metal cations such as Cu^{2+}, Mg^{2+}, and Ca^{2+} [20,22–24]. In our previous studies, we demonstrated that a titanium alloy and polycaprolactone (PCL) scaffold coated with EGCG and Mg^{2+} reduced the apoptosis of hADSCs in oxidative environments and increased ROS scavenging compared with cells on uncoated substrates [20,25]. Among the polyphenols, TA, which is composed of poly galloyl glucose or poly galloyl quinic acid esters, demonstrated the strongest antioxidative effects due to the presence of multiple phenolic groups (10 galloyl moieties per molecule) [26]. For example, nanoparticles formed by an MPN between TA and Fe_3O_4 dramatically decreased apoptosis and increased the angiogenic potential of human umbilical vein endothelial cells (HUVECs) in an oxidative environment by effectively scavenging the generated ROS [23]. Furthermore, recent research has demonstrated that nanoparticles containing both calcium and TA can scavenge ROS and promote osteogenic differentiation in hADSCs [27]. However, the formability of osteoinductive TA nanoparticles, balancing the ROS scavenging effect against the cytotoxicity of the nanoparticle, the effect on the mechanical strength of the hydrogel, and cellular responses within the 3D microenvironment of the composite hydrogel have not been investigated.

Given that, we hypothesized that a multifunctional composite GelMA hydrogel that not only promotes the osteogenesis of encapsulated stem cells but also enhances cell viability by ROS scavenging would be an effective material for stem cell encapsulation intended for bone regeneration. Therefore, we prepared multifunctional nanoparticles composed of TA and SBF minerals, assessing their effectiveness for ROS scavenging and osteoinduction, respectively, within a 3D cell-laden environment. We evaluated the potential of these nanoparticles within hydrogels by confirming enhanced stem cell viability, proliferation, migration, and osteogenesis. In addition, we evaluated the *in vivo* osteogenesis of the encapsulated stem cells and the responses of host cells adherent to the hydrogels.

2. Materials and methods

2.1. Materials

Sodium chloride (NaCl), magnesium chloride ($MgCl_2$), and sodium hydroxide (NaOH) were purchased from Junsei (Tokyo, Japan). Calcium chloride ($CaCl_2$) was obtained from DUKSAN (Kyungki-do, Korea). Sodium bicarbonate ($NaHCO_3$), potassium chloride (KCl), potassium bromide (KBr), sodium phosphate dibasic (Na_2HPO_4), silver nitrate, sodium thiosulfate, formalin solution, Folin-Ciocalteu reagent, sodium carbonate (Na_2CO_3), TA, thiazolyl blue tetrazolium bromide (MTT), ascorbic acid, 3 % hydrogen peroxide (H_2O_2), iron (III) chloride hexahydrate ($FeCl_3{\cdot}6H_2O$), 1,10-phenanthroline, 2,2-diphenyl-1-picrylhydrazyl (DPPH), 2,2′-azino-bis(3-ethylbenzothiazoline-6-sulfonic acid) diammonium salt (ABTS), alkaline phosphatase yellow liquid, alizarin red S, 2′,7′-dichlorofluorescein diacetate (DCFDA), 2-hydroxy-2-methylpropiophenone, dimethyl sulfoxide, and cetylpyridinium chloride were purchased from Sigma Aldrich (St. Louis, MO, USA). A QuantiChrom™ calcium assay kit was purchased from Bioassay Systems (Hayward, CA, USA). Phosphate-buffered saline (PBS) and Dulbecco's phosphate buffered saline (DPBS) were purchased from Welgene (Gyeongsan-si, Korea). Penicillin-streptomycin (PS) and trypsin/EDTA were purchased from Wisent (St. Bruno, QC, Canada). Dulbecco's modified Eagle's medium, MesenPRO RS™ medium, and fetal bovine serum (FBS) were purchased from Gibco BRL (Carlsbad, CA, USA). StemPro™ hADSCs, L-glutamine, a LIVE/DEAD® assay kit, Alexa Fluor™ 488 Phalloidin, CellROX green reagent, and anti-mouse IgG secondary antibody Texas red were purchased from Invitrogen (Carlsbad, CA, USA). GelMA, a UV spot-curing system, and 4 % paraformaldehyde were acquired from 3D Materials (Busan, Korea), UV SMT (Bucheon, Korea), and FUJIFILM Wako Pure Chemical Corporation (Richmond, VA, USA), respectively. Mounting medium containing DAPI and FITC-streptavidin were obtained from Vectashield® (Burlingame, CA, USA) and eBioscience (San Diego, CA, USA), respectively. For the *in vitro* experiments, hematoxylin and eosin (H&E) were purchased from BBC Biochemical (Mount Vernon, MA, USA). Maxime RT Premix and SYBR Premix Ex Taq were obtained from Intron (Seoul, Korea) and TAKARA (Otsu, Shiga, Japan), respectively. Primary antibodies for human anti-nuclei antibody (HNA), osteocalcin (OCN), and osteopontin (OPN) were purchased from Abcam (Cambridge, UK).

2.2. Preparation and characterization of tannic acid mineral nanoparticles

Tannic acid mineral nanoparticles (TMNs) were prepared as previously described [27]. Briefly, TA was dissolved in 30 mL of 10 X SBF solution (58.4 g of NaCl, 0.4 g of KCl, 3.7 g of $CaCl_2$, 1.0 g of $MgCl_2$, and 1.4 g of Na_2HPO_4 in 1.0 L of distilled water (DW), pH 4.4), and then 100.8 mg of $NaHCO_3$ (0.04 M) was added to the solution and stirred for 10 min to prepare TA mineral nanoparticles (TMNs; nominated as TMN-1, TMN-2, and TMN-3 using 0.5, 1.0, and 5.0 mg/mL TA, respectively). Each solution was centrifuged at 4000 rpm for 5 min, sequentially washed with tris-HCl buffer (pH 8.8) and DW, and lyophilized before use. The surface morphology of the TMNs was observed using a field emission scanning electron microscope (FE-SEM) (JSM 7600F, JEOL, Tokyo, Japan). The size (diameter) of the TMNs was measured from the images using ImageJ software. To quantify the total phenol content of the particles, 1 mg/mL of TMNs was dispersed in DW by a Sonifier® (BRANSON, St. Louis, MO, USA) and sequentially mixed with the same volume of Folin-Ciocalteu reagent for 10 min and the 600 μL of 2.0 % sodium carbonate for 1 h at room temperature (RT). The absorbance of the solution at 760 nm was measured using a spectrometer (Varioskan LUX, Thermo Scientific; Waltham, MA, USA). The anti-oxidative property of each particle was analyzed using ferric reducing antioxidant power, Fe conversion, DPPH, and ABTS radical scavenging assays. For the Fe conversion assay, the particles were immersed in 1 mL of Fe (III) solution (1.0 mg/mL 1,10-phenanthroline and 1.0 mM $FeCl_3$ in DW) for 20 min. The optical density of each of those samples at 510 nm was measured using the spectrometer for the ferric-reducing antioxidant power assay. The values were used to compare the conversion ratio of Fe (III) (%) with that of the ascorbic acid standard (0 % for 0 mg/mL and 100 % for 1.0 mg/mL ascorbic acid). For the DPPH assay, the particles were immersed in 1 mL of DPPH radical solution (0.1 mM DPPH in 80 % methanol) for 20 min (37 °C), and then the optical density of each sample solution at 520 nm was measured

using the spectrometer. Those values were used to compare the conversion ratio of DPPH radicals (%) with that of the ascorbic acid standard (0 % for 0 mg/mL and 100 % for 1.0 mg/mL ascorbic acid). For the ABTS radical inhibition assay, the particles were immersed in 1 mL of ABTS radical solution (7.0 mM ABTS and 2.4 mM potassium persulfate ($K_2S_2O_8$) in PBS). The optical densities of each sample at 732 nm were measured after 0 and 10 min using the spectrometer, and the scavenging ratio was calculated. The calcium content of the TMNs was measured using the QuantiChrom™ calcium assay kit (BioAssay Systems; Hayward, CA, USA). 1 mg of each particle was dissolved in 0.6 N of HCl for overnight at 37 °C and reacted with calcium assay reagent for 3 min and measured the absorbances at 612 nm using the spectrometer. To evaluate the release of calcium ions from the nanoparticles, the particles were incubated in DPBS at 37 °C for 1, 2, 3, 4, and 5 days, with DPBS samples collected and replaced at each time point.

2.3. Biocompatibility and anti-oxidative effect of TMNs

The hADSCs were cultured in growth medium (MesenPro RS medium supplemented with 2 % serum, 1 % PS, and 1 % L-glutamine) under standard culture conditions (37 °C, 5 % carbon dioxide (CO_2), 99 % humidity). Cells with a passage number of 5 or 6 were used in this study, and the medium was refreshed every 2 days. To confirm the biocompatibility of the nanoparticles, 1×10^4 cells were seeded into each well of a 24-well plate, and after 24 h, Transwell® (Corning, Lowell, MA, USA) inserts loaded with various concentrations (0, 10, 20, and 40 μg/mL) of TMN-2 were placed on the wells. The LIVE/DEAD® assay kit was used after 1 or 3 days, and the stained cells were observed through a fluorescence microscope (TE 2000, Nikon; Tokyo, Japan). The cells were also reacted with MTT solution (5 mg/mL MTT in DPBS) for 1 h, and the optical density of each sample at 550 nm was measured using the spectrometer. For the DCFDA assay, 2×10^4 cells were seeded in a 24-well plate for 24 h, and then the culturing medium was replaced with 100 μL of DCFDA solution (25 μM in PBS) for 45 min and then with conditioned medium with or without H_2O_2 (0.5 mM) and TMN-2 (40 μg/mL) for 30 min. Fluorescence images were captured by the fluorescence microscope, and the intensities of the samples at 485 nm (excitation) and 535 nm (emission) were measured with the spectrometer.

2.4. Preparation and characterization of TMN incorporated GelMA hydrogels

The GelMA solution (7.5 % in DPBS) incorporating 0, 1, 2, and 4 mg/mL of TMN-2 and 0.1 % (v/v) of 2-hydroxy-2-methylpropiophenone (photo-initiator) was dispensed into a custom-made polytetrafluoroethylene mold (8 mm diameter, 2 mm depth, 100 μL volume, and cylindrical shape) and irradiated using a UV curing system (400 mW/cm^2, 3 min) to prepare the GelMA composite hydrogels, which were denoted as G-TMN0–G-TMN4 depending on the concentration of particles. Optical images of each hydrogel were analyzed, and cross-sectioned SEM images were obtained after lyophilization to define the internal pore structure and area. Furthermore, SEM images clearly visualized the morphology of the nanoparticles and cells incorporated in the hydrogel, with nanoparticles and cells distinguished in orange and purple, respectively, to clarify their distribution and interaction. The pore area was calculated using ImageJ. The weights of hydrogels swollen with DPBS and dried were measured to calculate the swelling ratio (Swelling ratio (%) = (weight of swollen hydrogel – weight of dried hydrogel)/weight of dried hydrogel × 100). The storage moduli of the hydrogels were measured using a rheometer (HR10, TA Instruments; New Castle, DE, USA) under 1 % strain and 0.5 N of axial force. The hydrogels were treated with each reagent for the ferric-reducing antioxidant power and DPPH assays following the procedures described above to investigate their radical scavenging activity.

2.5. Encapsulation and viability of hADSCs within the composite hydrogel

Next, 5.0×10^5 cells/mL of hADSCs (100 μL hydrogel) were mixed with GelMA and various concentrations of TMNs, and the cell-encapsulating composite hydrogels were prepared following the previous gelation processes. Prior to each experiment, the cell-laden hydrogels were cultured in a 24-well plate with 1 mL of culture medium (MesenPro RS medium) that was refreshed every other day. The storage modulus of each hydrogel cultured for 1 or 7 days was quantified by the rheometer in the same conditions as before. The viability of the hADSCs in each hydrogel was calculated after culturing for 1 and 7 days by quantifying the live cells in fluorescent images after completion of the LIVE/DEAD assay (cell viability (%) = (number of live cells/total number of cells) × 100). The assay was conducted as previously described. The effects of UV irradiation time on the viability of the encapsulated cells and the mechanical properties of the hydrogel were investigated after UV crosslinking for 1 or 10 min and culturing the hydrogels for 1 or 7 days. For the F-actin staining, hydrogels encapsulating hADSCs were cultured for 1, 7, and 14 days; fixed in 4 % paraformaldehyde; washed in PBS; reacted with Alexa Fluor™ 488 Phalloidin (1:100 in PBS) at 37 °C for 1 h; and mounted with mounting medium containing DAPI. The hydrogels were then observed using a confocal microscope (TCS SP5, Leica; Wetzlar, Germany).

2.6. Anti-oxidative effects of TMNs on hADSCs encapsulated within the composite hydrogel

Stem cell–laden hydrogels were cultured in conditioned medium containing H_2O_2 (0, 0.5, and 1 mM) for 1 or 7 days to confirm the protection of cells by nanoparticles from the apoptosis caused by H_2O_2. The hydrogels were fixed in 4 % paraformaldehyde and then paraffinized after serial dehydration (immersion in 70–100 % EtOH and xylene). Subsequently, the hydrogels were sectioned into 5 μm thicknesses by a microtome (Leica Biosystems GmbH; Wetzlar, Germany), hydrated following the reverse steps of dehydration to stain them with the enzyme terminal deoxynucleotide transferase for 1 h, washed with PBS, and mounted with mounting medium containing DAPI. The stained samples were observed using the fluorescence microscope, and the TUNEL-positive cells were counted (TUNEL-positive cells (%) = (number of TUNEL-positive nuclei/total number of nuclei) × 100). LIVE/DEAD staining was also performed as described above. Additionally, the intracellular oxidative stress level of the cells encapsulated in the composite hydrogels was measured using the fluorescent microscope after incubating the samples in CellROX staining solution (5.0 μM in medium) for 1 h at 37 °C. The relative fluorescence intensity in the images was measured using ImageJ. For real-time quantitative polymerase chain reaction (RT-qPCR) analysis, the cell-encapsulating composite hydrogels were reacted with 200 CDU/mL collagenase solution for 1 h at 37 °C to completely dissolve the hydrogels. The supernatant was removed after centrifugation (1200 rpm for 3 min) to obtain the cells, and the mRNA was extracted from the cells using an RNeasy Mini Kit (Qiagen; Hilden, Germany). The quantity was measured using a NanoDrop 2000 (Thermo Scientific; Waltham, MA, USA). cDNA was synthesized by adding 1 μg of mRNA and diethyl pyrocarbonate (DEPC)-treated water to a cDNA polymerization kit (total volume: 20 μL) (Maxime RT PreMix kit, iNTRON Biotechnology; Seoul, Korea). Then, 2 μL of cDNA solution was mixed with 0.4 μL of SYBR reagent, 0.4 μL of ROX reference dye (50 ×), 6.8 μL of DEPC-treated RNA-free water, and 0.4 μL of target-specific gene primers and processed with RT-qPCR (StepOnePlus Real-Time PCR System, Applied Biosystems; Foster City, CA, USA) for amplification during 40 cycles of annealing at 95.0 °C for 15 s, extension at 60.0 °C for 60 s, and a melting curve stage at 60.0 °C–95.0 °C in increments of 0.5 °C per 5 s. The sequences of primers (COSMO Genetech; Seoul, Korea) used in this experiment is listed in Table S1.

2.7. In vitro osteogenic differentiation of hADSCs encapsulated within the composite hydrogel

For investigation of osteogenic differentiation, G-TMN0 and G-TMN2 were prepared while changing the encapsulated cellularity to 2.0×10^6 cells/mL (100 μL in each hydrogel) and UV irradiation time (400 mW/cm^2) to 20 and 60 s, respectively, to equalize the mechanical properties for the groups. To measure the calcium content, hydrogels that had been cultured for 14 days were dissolved in collagenase solution according to the procedure described above, and after removing the supernatant, the calcium assay reagents were added and left for 3 min. The absorbance at 612 nm was detected by the spectrometer. The hydrogels were fixed in 4 % paraformaldehyde and stained using alizarin red S solution to visualize the calcium deposition, and cross-sectioned specimens of each hydrogel, made using the same paraffin embedding and sectioning processes described above, were also stained with alizarin red S solution. The optical images were captured by a camera and a phase contrast microscope. The stained hydrogels were then incubated with extraction buffer (100 μg/mL cetylpyridinium chloride, 10 mM Na_2HPO_4) to dissolve the stained calcium ions, and the absorbance at 550 nm was measured by the spectrometer. cDNA from G-TMN0 and G-TMN2 samples cultured for 7 or 14 days was synthesized using the RT-qPCR processes described above and sequences shown in Table S1. To assess the ALP activity, the hydrogels were dissolved using collagenase solution according to the procedure described above, and the cells were lysed with Pierce™ RIPA buffer (Thermo Fisher Scientific; Waltham, UK). The solution was reacted with a p-nitrophenyl phosphate solution for 30 min at 37 °C, and the absorbance at 405 nm was measured by the spectrometer after we stopped the reaction by adding 3.0 N NaOH to the solution. ALP activity is expressed as nmol of ALP per ng of DNA. The G-TMN0 and G-TMN2 samples cultured for 14 days were embedded in paraffin and cross-sectioned using the methods described above to conduct immunohistochemistry (IHC) staining for runt-related transcription factor 2 (RUNX2) and OPN. The specimens were sequentially hydrated, reacted with the solution of primary antibodies (anti-RUNX2 or anti-OPN, 1:100 in blocking buffer: 5 % FBS and 0.1 % Tween-20 in PBS) at 4 °C for 24 h, washed with PBS, reacted with anti-mouse IgG biotin-conjugated secondary antibody (1:100 in PBS) at 37 °C for 1 h, similarly washed, and reacted with FITC-conjugated streptavidin tertiary antibody (1:100 in PBS) at 37 °C for 1 h. The samples were then mounted with mounting medium containing DAPI and observed using the fluorescence microscope to calculate the ratio of RUNX2-positive or OPN-positive.

2.8. In vivo subcutaneous transplantation

Six-week-old female Balb/c nude mice (Institute for Cancer Research species, Narabiotech; Seoul, Korea) were used for the *in vivo* implantation of hydrogels into subcutaneous tissue (n = 6). The animal experiments were approved by the Institutional Animal Care and Use Committee of Hanyang University (approval number: 2022-0081A). The experimental groups were: without transplantation (control), G-TMN0 encapsulating 2.0×10^5 hADSCs (G-TMN0 w/cells), G-TMN2 without cells (G-TMN2 w/o cells), and G-TMN2 encapsulating 2.0×10^5 hADSCs (G-TMN2 w/cells). Each mouse was injected with 150 μL of anesthetic composed of Zoletil (60 mg/kg) and Rompun (20 mg/kg) before surgery. After sterilization with 70 % ethanol, a 2 cm incision was made on the middle of the dorsal skin. The hydrogels were transplanted one by one onto the right and left sides of the incision (two hydrogels per mouse). The incised skin was sutured and then treated with povidone-iodine for protection against infection. The mice were sacrificed by CO_2 suffocation eight weeks after surgery, and the hydrogel-transplanted tissues were harvested. The tissues were fixed in 10 % formalin for 24 h, placed in PBS, and stored at 4 °C for histological staining. For H&E staining, the samples were paraffinized and cross-sectioned following the methods described above (10 μm thicknesses), hydrated, and then stained with hematoxylin for 8 min and eosin for 4 min. For von Kossa staining, the same specimens were incubated in a 2 % silver nitrate solution under 60W light for 1 h at RT, immersed in 5 % sodium thiosulfate for 3 min, and then counterstained with eosin. The histological images were captured by the phase contrast microscope. IHC staining for OCN and OPN was conducted for these specimens following the protocols described above. For the human anti-nuclei antibody (HNA) staining, the specimens were sequentially hydrated, treated with the primary antibody solution (anti-HNA 1:100 in blocking buffer) at 37 °C for 1 h, washed, treated with anti-mouse IgG Texas red (1:100 in PBS) at 37 °C for 1 h, and mounted with mounting medium containing DAPI. Fluorescent images were observed using the fluorescence microscope. The specimens were frozen in liquid nitrogen, lysed in 1 mL of Trizol buffer for 24 h at 4 °C, mixed with agitation in 200 μL of chloroform, and centrifuged to obtain the transparent supernatant containing the nucleic acids. The previously stated mRNA extraction and RT-qPCR processes were applied to these samples using the same osteogenic primers as in the *in vitro* experiment.

2.9. Degradation of hydrogel

The same groups of composite hydrogels used in the *in vivo* experiment were reacted with 0.5 CDU/mL of collagenase solution for 0, 30, 60, 120, 180, and 270 min at 37 °C to monitor their degradation. Optical images of each hydrogel were obtained, and the weight of the hydrogel at each time point was measured after lyophilization (Mass loss (%) = (weight of hydrogel/weight of initial hydrogel) × 100). Additionally, the hydrogel was incubated at 37 °C with 0.2 CDU/mL of collagenase solution for 0, 1, 3, 6, 12, and 18 h, and the degradation of the hydrogel in DPBS at 37 °C was monitored. Furthermore, the amount of polyphenols and calcium ions released from the nanoparticles during the hydrogel degradation process was evaluated.

2.10. Statistical analysis

All quantitative data are expressed as the mean ± standard deviation of more than triplicate samples ($n \geq 3$). GraphPad Prism 7 software (San Diego, CA, USA) was used to conduct one-way analysis of variance with either Tukey's honest significant difference test (for more than two variables) or Student's t-test (for two variables). Significance is denoted as a P value < 0.05, and all experiments were independently repeated at least three times.

3. Results and discussion

In this study, we set out to develop a multifunctional composite hydrogel with improved cell viability, anti-oxidation, and osteogenesis for stem cell transplantation (Fig. 1). Nanoparticles self-assembled from TA and SBF biominerals were incorporated within a GelMA hydrogel, and the concentration of TA in the particles, number of particles in each hydrogel, and mechanical strength of the hydrogels were characterized to enhance both the ROS scavenging and osteogenic differentiation of hADSCs encapsulated in the hydrogel.

3.1. Synthesis and characterization of the tannic acid mineral nanoparticles

The TA nanoparticles showed stable amorphous shapes regardless of the TA concentration, but the color became gradually darker as the TA concentration increased (Fig. 2a), consistent with previous results [28]. The sizes of the TMNs also increased according to the concentration of TA (Fig. 2b). In our previous study, we found that nanoparticles composed of TA and SBF minerals became larger as the TA concentration increased, but saturated at 5.0 mg/mL, when the particle diameter was 400 μm [27]. The self-assembly of MPN-mediated polyphenols occurs continuously due to the LaMer mechanism, which continues until

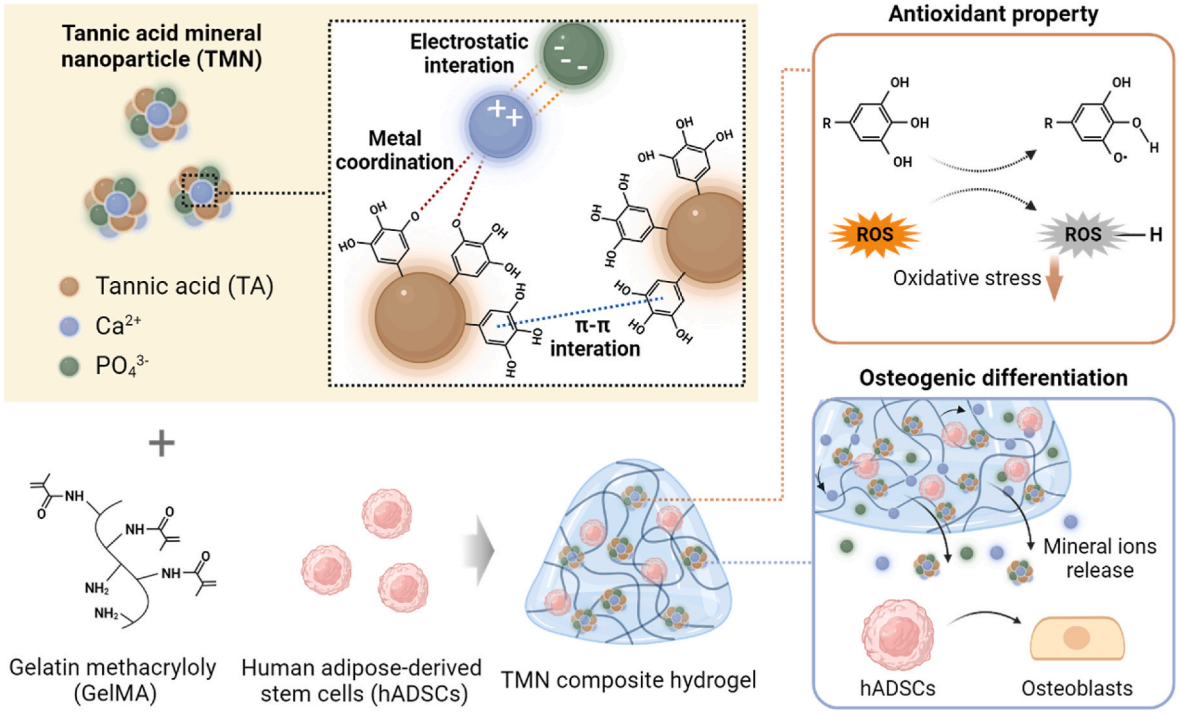

Fig. 1. Schematic illustration of the preparation of tannic acid mineral nanoparticles (TMNs) and composite GelMA hydrogels incorporating TMNs for the encapsulation of stem cells. TA and the minerals self-assembled through chemical reactions to form nanoparticles, and the TMNs in the composite hydrogel contributed to the antioxidant properties and osteogenic differentiation of encapsulated human adipose-derived stem cells.

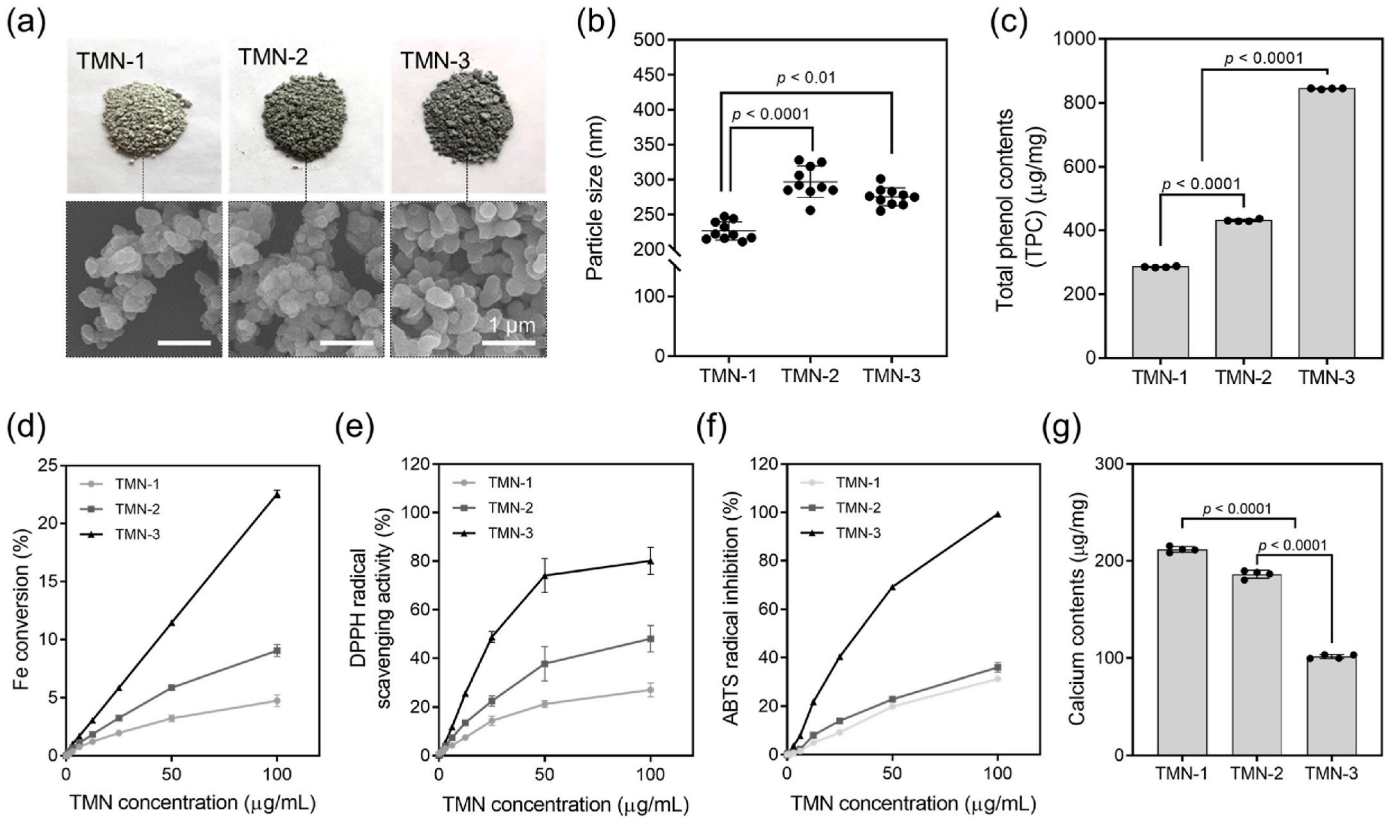

Fig. 2. Preparation and characterization of multifunctional nanoparticles. (a) Optical and SEM images of TMN-1, TMN-2, and TMN-3 (scale bar = 1 μm) prepared using various concentrations of tannic acid and (b) sizes (n = 8). (c) Total phenol content of the nanoparticles (n = 4). Radical scavenging effects of TMNs shown by the (d) ferric reducing antioxidant power assay, (e) DPPH assay, and (f) ABTS assay (n = 4). (g) The amount of calcium ions deposited by each nanoparticle (n = 4).

the free TA monomers are fully saturated and causes the size expansion of the particles as the concentration of TA increases [29]. The total phenol content (TPC) analysis demonstrated that, as more TA was incorporated within the particles, the concentration of TA became greater (Fig. 2c) and the ROS scavenging effects found in the Fe conversion, DPPH, and ABTS assays also increased according to TA concentration (Fig. 2d–f). These results suggest that the phenolic groups from TA were partially oxidized to form an MPN with the mineral ions, but the remaining polyphenol groups were still able to take part in ROS scavenging after the formation of the particle structure [30,31]. In contrast, it should be noted that the calcium contents in each particle were significantly decreased as the TA concentration increased (Fig. 2g) since more polyphenols reacted with the calcium ions in each particle as the TA concentration increased [30,32]. Collectively, our results show that the TMNs were successfully prepared by self-assembly processes that involved metal coordination, electrostatic interaction, and oxidative polymerization. In addition, the nanoparticles maintained excellent radical scavenging ability and the release profile showed that TMN-2 released significantly more calcium (15.5 ± 0.9 μM) compared to TMN-1 (9.4 ± 1.5 μM) and TMN-3 (9.8 ± 0.7 μM) (Fig. S1). In our characterization, the TMN-2 particles exhibited a reasonable mineral content as well as good ROS scavenging ability, so they were used for further investigations.

3.2. Biocompatibility and anti-oxidative effect of TMNs

We found that TMN-2 had no detrimental effect on the viability of hADSCs at any concentrations (0–40 μg/mL incorporating 10.1 μM TA) (Fig. 3a and b). An excessive amount of TA could induce extrinsic apoptosis because TA forms phenol–protein or –lipid complexes in the presence of oxygen, leading to overproduction of phenoxyl radicals and semiquinones that can damage mitochondria [33–35]. However, our results indicate that the TMN-2 particle structure is more favorable for cell viability than the same amount of TA in another form. As noted, increasing the amount of nanoparticles could lead to excessive TA release, which may be detrimental to cells, and thus, we carefully selected the concentration to be non-toxic to cells in our experiments. Biocompatibility tests were conducted using MTT assays with hADSCs. As demonstrated in Fig. 3b, cells cultured with TMN-2 at different concentrations exhibited enhanced absorbance compared to the control group, indicating the low cytotoxicity of TMN-2. The H_2O_2 was converted to H_2O within cells by metabolic activities while forming

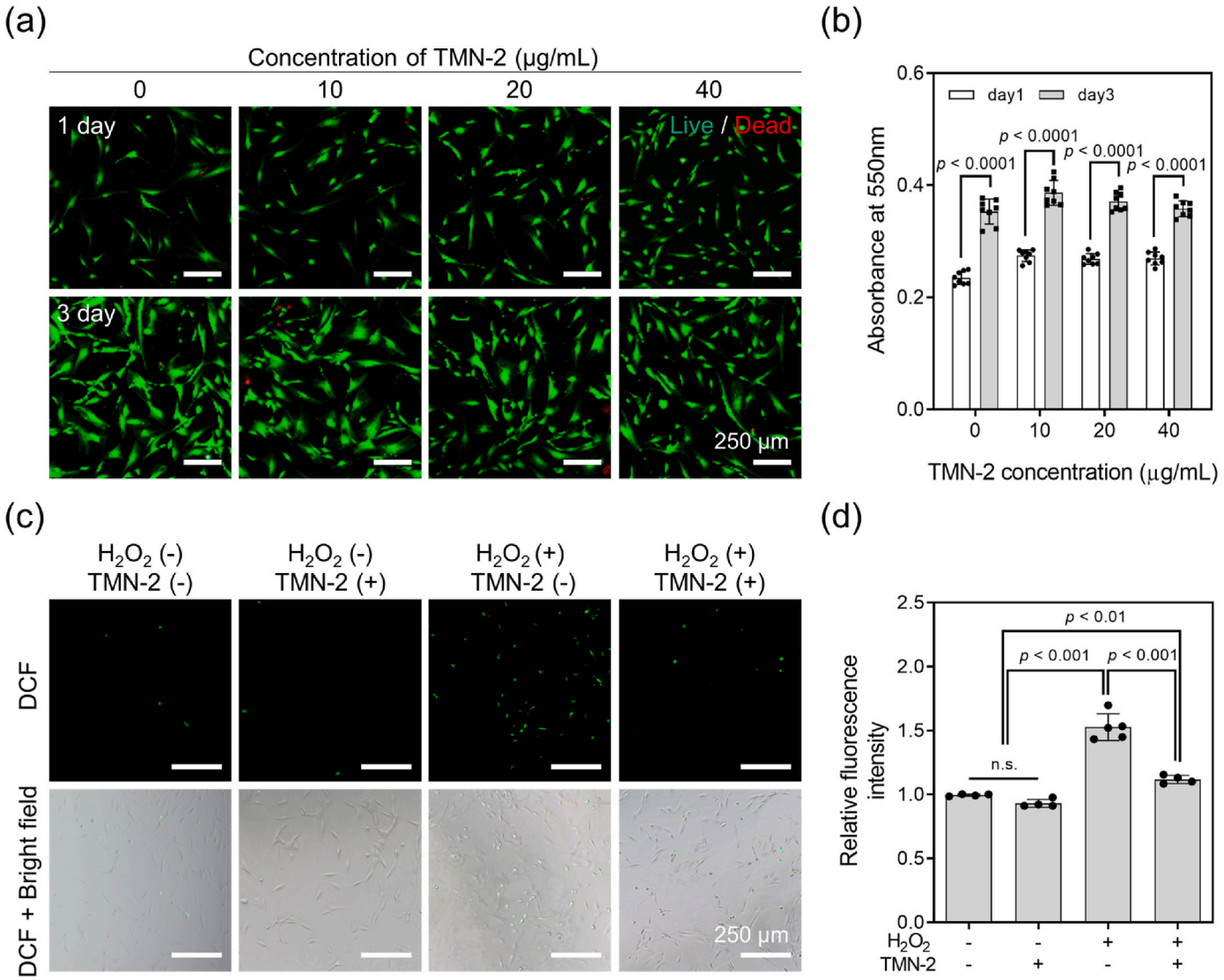

Fig. 3. Biocompatibility and radical scavenging effects of TMNs. (a) LIVE/DEAD staining and (b) MTT assay of hADSCs cultured with different concentrations of TMN-2 for 1 or 3 days (scale bar = 250 μm). (c) DCFDA assay images and (d) the relative fluorescence intensities of hADSCs cultured with and without H_2O_2 and TMN-2 (scale bar = 50 μm).

intracellular ROS that impair the nucleic acids [36]. The polyphenol groups in TA could have reduced the level of the intracellular ROS (DCF) in two ways; the TA could directly scavenge the ROS using phenolic groups, and it could indirectly eliminate ROS by upregulating the generation of intracellular anti-oxidative enzymes such as superoxide dismutase 1 and heme oxygenase 1 [37]. The DCF assay demonstrated that TMN-2 effectively reduced intracellular ROS under H_2O_2 stress (Fig. 3c). As seen in Fig. 3c, cells exposed to H_2O_2 lost their original shape and contracted into a rounded form. The treatment with TMN-2 alleviated the oxidative intracellular stress in the cells. Quantitative analysis showed that after H_2O_2 treatment, the relative fluorescence intensity increased by 1.6 ± 0.1 times, but decreased when TMN-2 was treated (Fig. 3d).

3.3. Preparation and characterization of composite GelMA hydrogels with TMNs and hADSCs

Various concentrations of TMN-2 were incorporated within GelMA hydrogels to form composite hydrogels and analyze the cellular responses (Fig. 4a). As the concentration of TMN-2 in the hydrogels increased, the color of the hydrogels became darker (Fig. 4b), the pore size and swelling ratio increased, and the storage moduli decreased (Fig. 4b–e). For example, the swelling ratios of G-TMN0 and G-TMN4 were 9.9 ± 0.6 and 14.1 ± 1.1 %, respectively, and their storage moduli were 1194.0 ± 23.5 and 372.6 ± 40.9 Pa (Fig. 4d and e). The presence of polyphenols could reduce the free radicals used for cross-linking the hydrogel during gelation, so the concentration-dependent increase in pore size and swelling ratio and decrease in the mechanical strength of the hydrogels are attributed to the presence of TMNs [38]. Similar results were also found in composite hydrogels incorporating other polyphenols. For example, incorporating of EGCG in a composite hydrogel increased the pore size as well as swelling ratio, and decreased the mechanical strength depending on the concentration of EGCG [39]. In the DPBS, the hydrogel degradation experiments showed a reduction of 15.8 ± 2.6, 25.0 ± 2.5 % in the initial dry weight of the hydrogels over 14 days, with complete degradation under collagenase treatment within 18 h. These results indicate that the uniformly dispersed nanoparticles in the hydrogels are released alongside the degradation of the hydrogel, and the released phenol induces antioxidant effects in the microenvironment. In our study, incorporating more TMNs in the hydrogel increased the ROS scavenging effects, as demonstrated by the Fe conversion and DPPH assays (Fig. 4f and g).

3.4. Encapsulation and viability of hADSCs within the composite hydrogel

Generally, the excessive amounts of residual ROS generated during photo-polymerization of GelMA can lead to apoptosis, disruption of homeostasis, and DNA mutation [40]. Such cellular damage could be effectively mitigated by eliminating ROS [41,42]. Similarly, we found that the viability of hADSCs encapsulated within the hydrogel increased as the concentration of TMN-2 in the hydrogel increased, even though the storage modulus of hydrogel decreased (Fig. 5a–c). The LIVE/DEAD assay detected a significant level of dead signals in the G-TMN0 and G-TMN1 after 7 days of culture, whereas few dead signals were found in the G-TMN2 and G-TMN4 (Fig. 5c). The cells in the G-TMN2 maintained their viability during 7 days of culture, and the cells in the G-TMN4

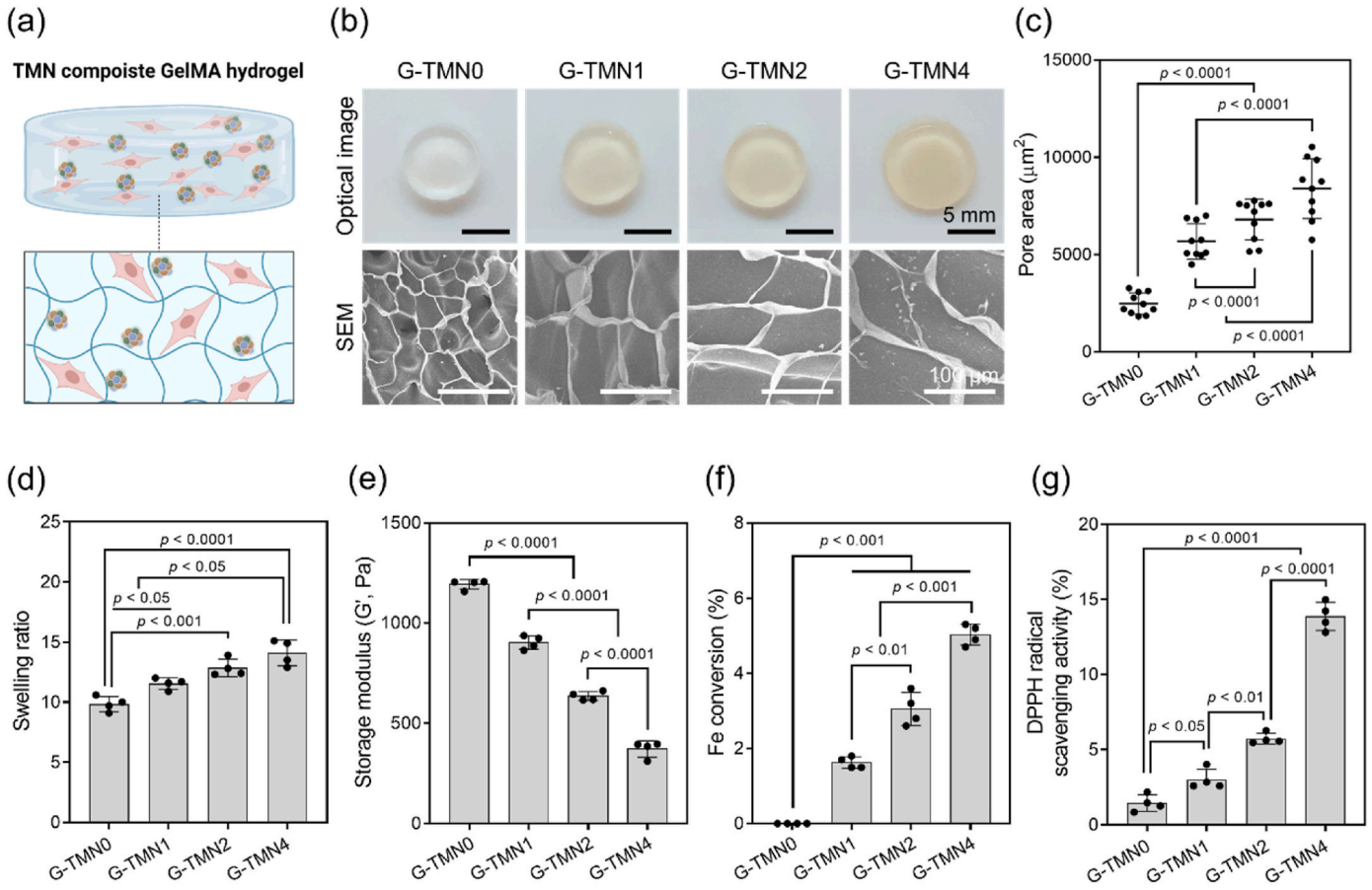

Fig. 4. Preparation and characterization of a GelMA hydrogel incorporating TMNs. (a) Schematic illustrations of the TMN-incorporated hydrogel with encapsulated hADSCs. (b) Optical (scale bar = 5 mm) and (c) SEM images (scale bar = 100 μm) of G-TMN depending on the concentration of incorporated TMN. Characterizations from each hydrogel: (c) pore area (n = 10), (d) swelling ratio (n = 4), and (e) storage moduli (n = 4). The radical scavenging effect of each hydrogel: (f) ferric reducing antioxidant power (n = 4) and (g) DPPH radical scavenging activity (n = 4).

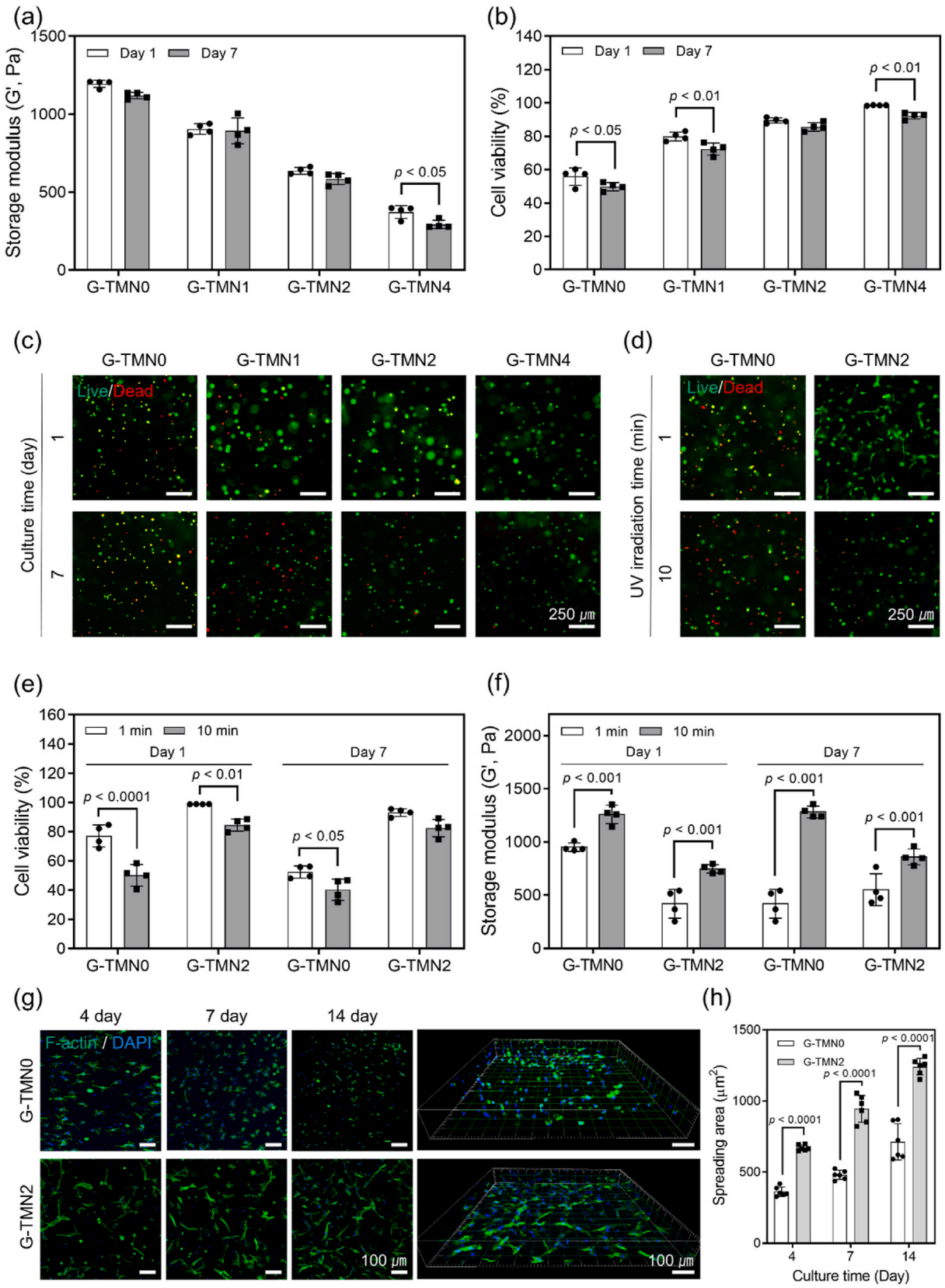

Fig. 5. Encapsulation and viability of hADSCs within the composite hydrogel. (a) Storage moduli and (b) cell-viability of G-TMN0, G-TMN1, G-TMN2, and G-TMN4 hydrogels encapsulating hADSCs after culturing for 1 or 7 days (n = 4). (c) LIVE/DEAD staining of cells within each hydrogel (scale bar = 250 μm). (d) LIVE/DEAD staining of cells encapsulated in G-TMN0 and G-TMN2 under 1 or 10 min of UV exposure (scale bar = 250 μm). (e) Cell viability and (f) storage moduli of each hydrogel after culturing for 1 or 7 days (n = 4). (g) F-actin-stained confocal microscopic images of cells in G-TMN0 and G-TMN2 with identical mechanical strength after culturing for 4, 7, and 14 days (scale bar = 100 μm) and (h) their quantified spreading area at each time point (n = 6).

showed only a slight decrease in viability (Fig. 5b). The initial cell viability in the G-TMN4 was increased on day 1 due to the ROS scavenging effect, but the over-provided TMNs might have eliminated even the biological radicals generated during adenosine triphosphate synthesis from mitochondria during the next 7 days, leading to partial decrease in cell-viability [43]. Similar tendency was also found in the previous study that ADSCs encapsulated in TA-incorporated collagen hydrogel revealed that the cell viability increased with the incorporated concentration of TA; however, the viability was decreased when the amount of TA in the hydrogel was greater than 5 wt% [33]. Thus, we selected the G-TMN2 group for the further analyses.

In the G-TMN0 hydrogels, the dead signals in the LIVE/DEAD assay were increased with increase of the UV exposure time from 1 to 10 min, but that change was not detected in the G-TMN2 (Fig. 5d and e). The hydrogels with 10 min of UV exposure showed improved mechanical properties compared with those cured for 1 min (Fig. 5f). When we initially prepared G-TMN0 and G-TMN2 to have the same mechanical strength, we found that the incorporation of TMN-2 also enhanced cell migration (Fig. 5h). The F-actin staining confirmed that the cells in G-TMN2 spread farther and showed more frequent spindle and elongated

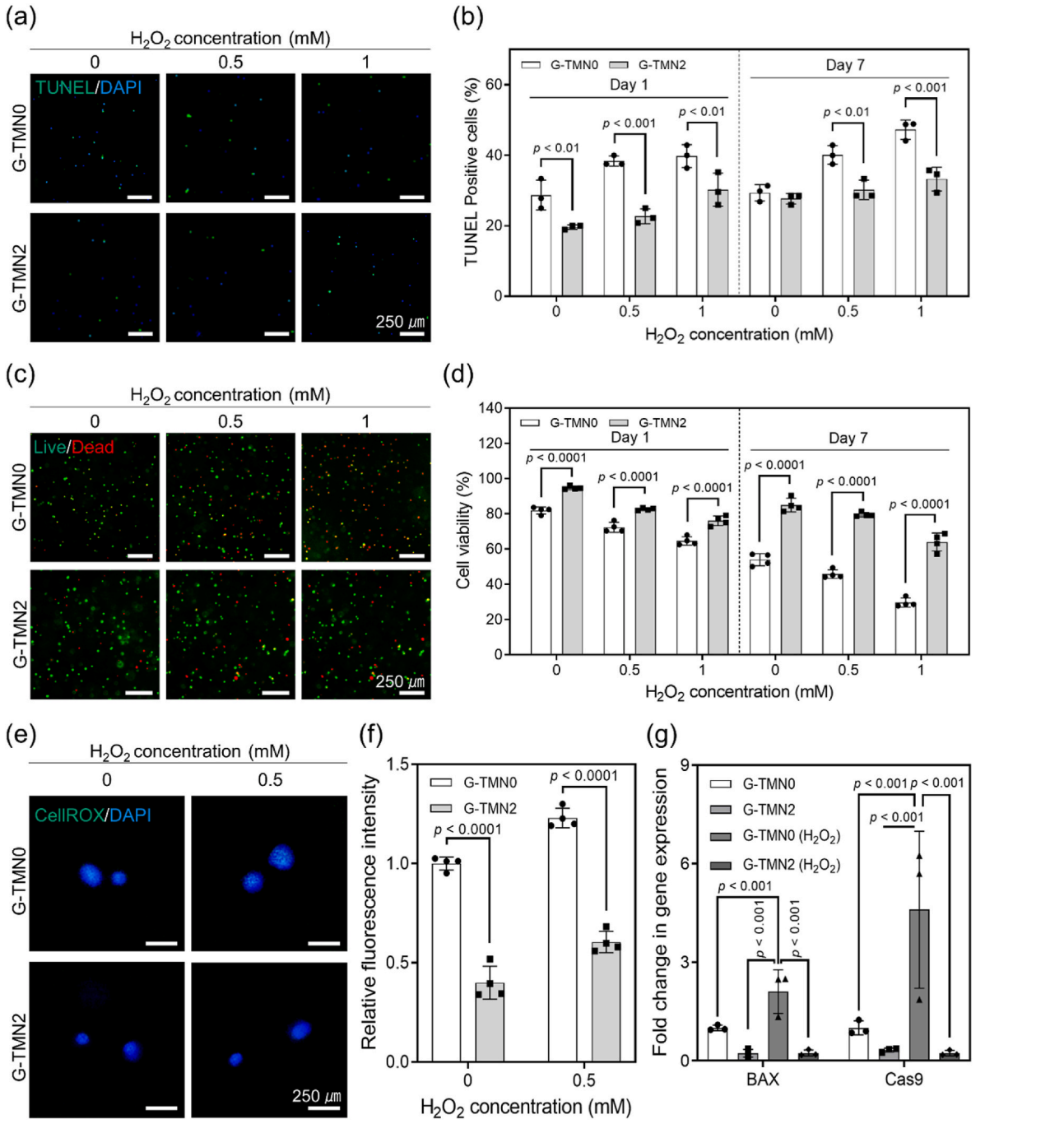

Fig. 6. Anti-oxidative effects of TMNs on hADSCs encapsulated within the composite hydrogel. (a) Apoptotic signals from cells encapsulated within G-TMN0 and G-TMN2 under 0.0, 0.5, and 1.0 mM H_2O_2 (TUNEL assay, scale bar = 250 μm) and (b) quantified TUENL-positive nuclei from each group after culturing for 1 or 7 days (n = 3). (c) LIVE/DEAD staining images of cells from each group (scale bar = 250 μm) and (d) quantified cell viabilities after culturing for 1 or 7 days (n = 4). (e) Fluorescent images from CellROX staining of cell-laden hydrogels under 0.0 and 0.5 mM H_2O_2 (scale bar = 250 μm) and (f) quantified fluorescence intensities after culturing for 2 days (n = 4). (g) Apoptosis-related gene expression of cells from each group after culturing for 2 days (n = 4).

morphology than those in G-TMN0, with quantified areas as 713 ± 128 and 1241 ± 58 μm^2, respectively, after 14 days of culture (Fig. 5h). The similarity in the mechanical strength of the hydrogels indicates that they possessed similar gel networks, pore sizes, and matrix compositions, but the cell-adhesive catechol and pyrogallol groups in the polyphenol might have increased cell migration and proliferation through deposition of fibronectin and initiation of the integrin-mediated focal adhesion kinase signaling pathway [20,34]. Similar to our results, HUVECs and fibroblasts loaded on a polydopamine-coated PCL scaffold and a hydrogel containing TA and EGCG, respectively, showed doubled cell migration and proliferation compared with cells on scaffolds without polyphenols [35,44]. Taken together, the results suggest that the G-TMN2 hydrogels effectively increased both the viability and the spread of encapsulated cells by resisting ROS generated during photo-polymerization (Fig. 5).

3.5. *Anti-oxidative effects of TMNs on hADSCs encapsulated within the composite hydrogel*

Oxidative stress induces intercellular ROS production and increases the expression of pro-apoptotic genes such as BAX and caspase, leading to hypodiploid cells, DNA fragmentation, and mitochondrial damage

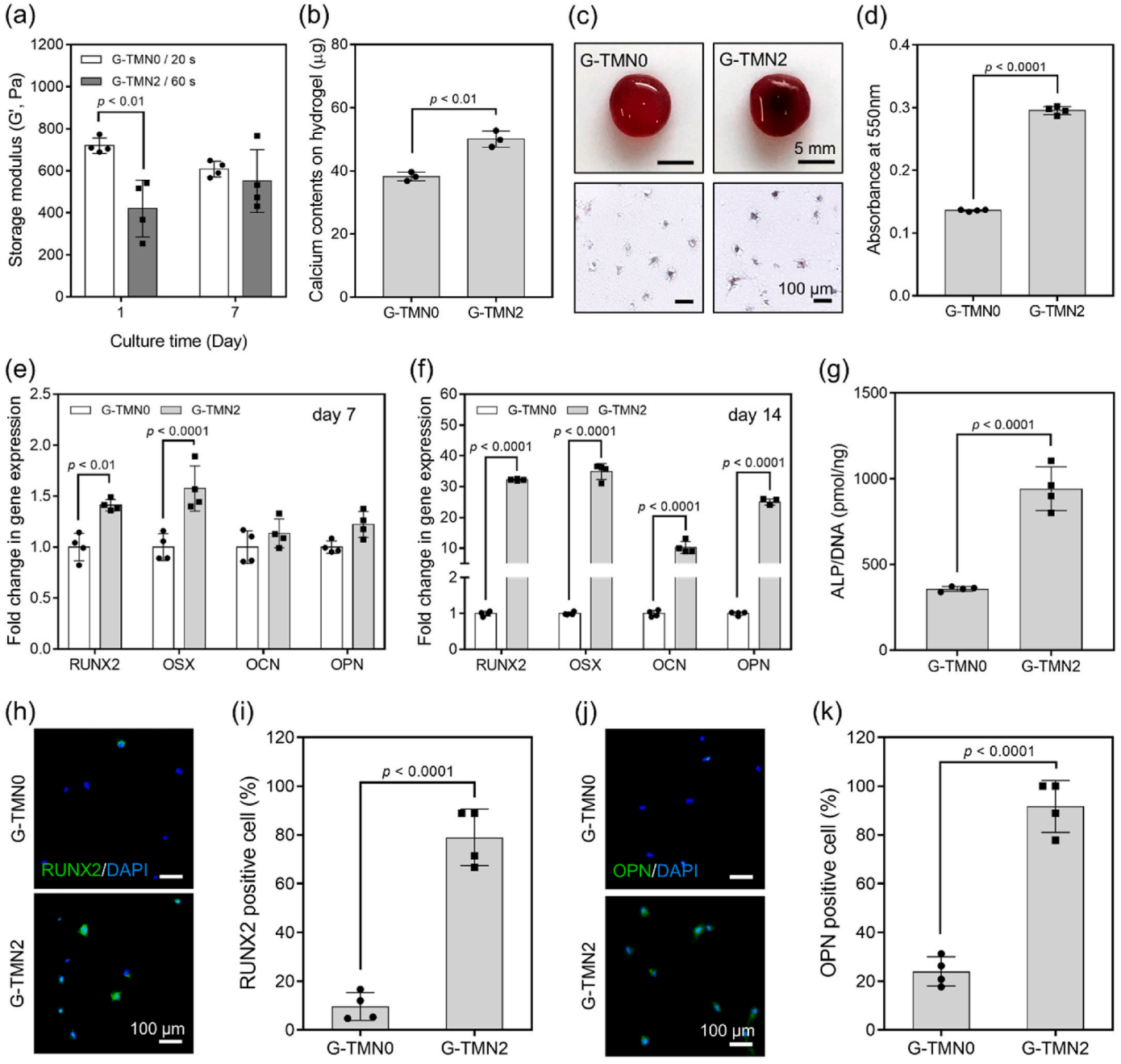

Fig. 7. *In vitro* osteogenic differentiation of hADSCs encapsulated within the composite hydrogel. (a) Storage moduli of G-TMN0 and G-TMN2 under 20 and 60 s of UV exposure, respectively, and culturing for 1 or 7 days (n = 4). (b) Calcium content deposited on the hydrogels (n = 3) and (c) alizarin red S staining from entire hydrogels (scale bar = 5 mm) and horizontally cross-sectioned hydrogels (scale bar = 100 μm) after culturing for 14 days. (d) Quantitative analysis of alizarin red S from the hydrogels (n = 4). Osteogenic gene expression of cells from each hydrogel after culturing for (e) 7 or (f) 14 days (n = 4). (g) ALP activity from each hydrogel after culturing for 7 days (n = 3). (h) RUNX2 IHC staining of horizontally sectioned G-TMN0 and G-TMN2 (scale bar = 100 μm) and (i) the ratio of RUNX2-positive cells (n = 4). (j) OPN IHC staining of horizontal sections from each hydrogel (scale bar = 100 μm) and (k) the ratio of OPN-positive cells (n = 4).

[43]. Polyphenols can increase cell viability because they effectively scavenge intracellular ROS and directly reduce exogeneous H_2O_2 [45]. The TUNEL assay showed fewer apoptotic nuclei in cells in G-TMN2 than in those in G-TMN0 when they were cultured for 7 days in conditioned medium treated with H_2O_2 (Fig. 6a and b). Consistently, the number of dead signals in G-TMN2 was dramatically lower than in G-TMN0 (Fig. 6c and d). For example, the numbers of cells with positive dead signals in G-TMN0 and G-TMN2 under 1 mM H_2O_2 were 45.8 ± 2.4 and 29.6 ± 2.5 %, respectively (Fig. 6d). The CellROX assay showed that the cells in G-TMN0 had a larger amount of intracellular ROS than those in G-TMN2 (Fig. 6e and f). The RT-qPCR analysis demonstrated that the expression of apoptosis-related genes (BAX and Cas9) in the cells in G-TMN0 increased under 0.5 mM H_2O_2, whereas that in the cells in G-TMN2 did not change significantly after H_2O_2 treatment (Fig. 6g). Therefore, our results show that both intracellular and extracellular ROS are detrimental to cells within a hydrogel, and the G-TMN2 hydrogels dramatically improved the viability of encapsulated stem cells by mitigating oxidative stress (Fig. 6).

3.6. *In vitro* osteogenic differentiation of cells encapsulated within the composite hydrogel

To investigate the effect of nanoparticles on the osteogenic differentiation of hADSCs encapsulated within hydrogels, we formed G-TMN0 and G-TMN2 samples with matched mechanical strengths to minimize the influence of mechanical properties on stem cell differentiation [34]. The storage moduli of the G-TMN0 (20 s of UV exposure) and G-TMN2 (60 s of UV exposure) samples used in this experiment were similar on day 7 (Fig. 7a). The hADSCs encapsulated in G-TMN2 showed greater calcium deposition than those in G-TMN0 (Fig. 7b–d). RT-qPCR

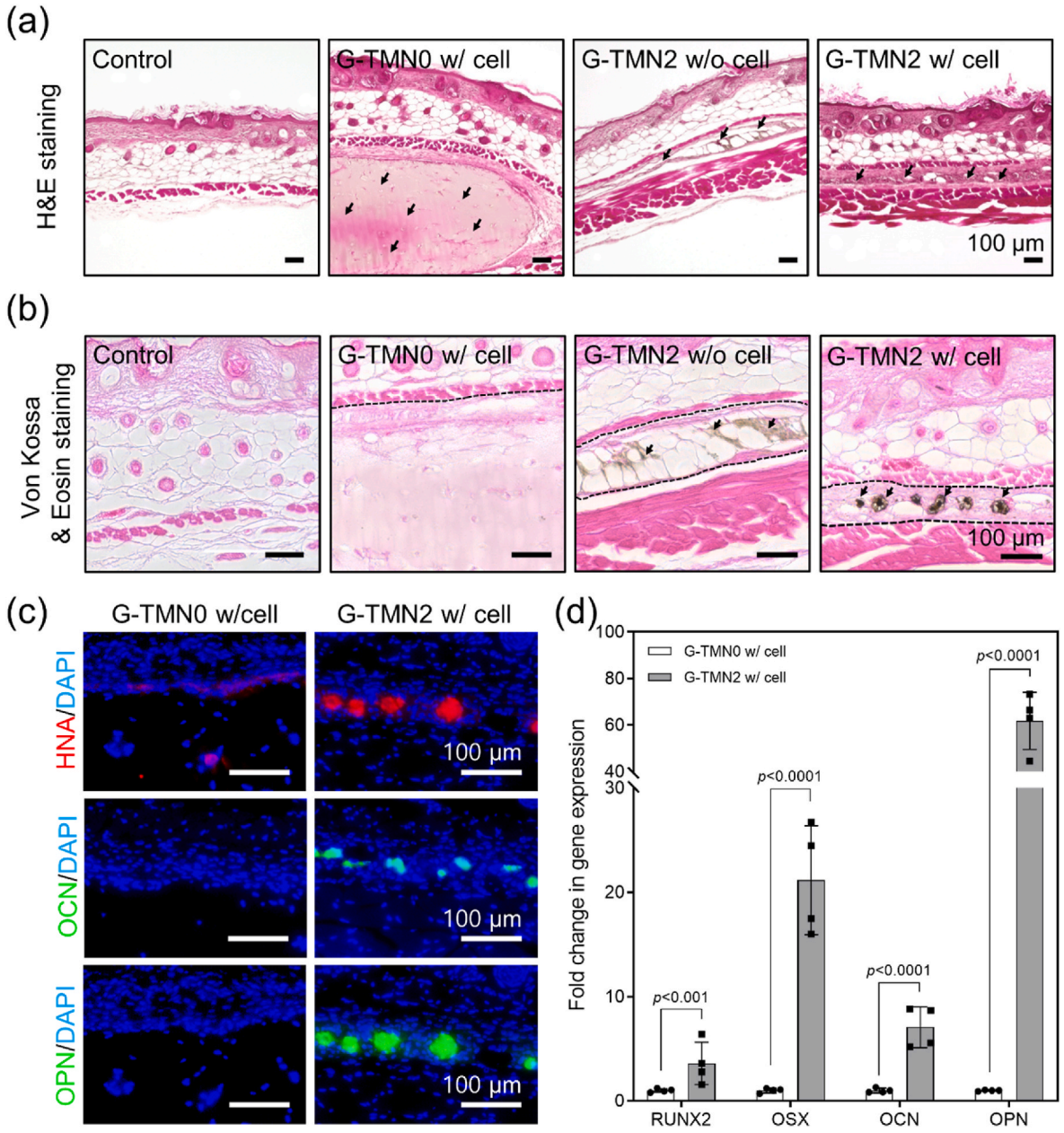

Fig. 8. *In vivo* subcutaneous transplantation of composite hydrogels. (a) H&E staining images of subcutaneous tissues harvested from the control, G-TMN0 w/cell, G-TMN2 w/o cell, and G-TMN2 w/cell groups (black arrows indicate hydrogel, scale bar = 100 μm) and (b) von Kossa and eosin staining images from each group (black arrows indicate the minerals deposited in the hydrogel). (c) HNA, OCN, and OPN IHC staining of tissues harvested from the G-TMN0 w/cell and G-TMN2 w/cell groups (scale bar = 100 μm). (d) Osteogenic gene expression of hADSCs from each group (n = 4).

confirmed that the cells in G-TMN2 showed increased osteogenic gene expression and ALP activity compared with those in G-TMN0 (Fig. 7e–g). The IHC staining similarly showed an 8.1- and 3.8-fold increase in RUNX2-and OPN-positive cell, respectively, for the cells in G-TMN2 compared with those in G-TMN0 (Fig. 7h–k). The increased osteogenic differentiation of cells within G-TMN2 might indicate that the calcium phosphate ions in the TMNs activate the ERK 1/2, PI3K/Akt, and IGF-1 signaling pathways, which lead to osteogenesis of stem cells [20]. Similar to our results, hydrogels containing calcium phosphate particles have previously been used to induce osteogenic differentiation of cells [46–48]. For example, MC3T3 cells (pre-osteoblasts) within a GelMA hydrogel containing 25 mg of hydroxyapatite particles showed 3 times greater ALP activity than cells within a hydrogel without particles, and bone marrow-derived mesenchymal stem cells (BMSCs) within an alginate hydrogel containing bioactive glass–based particles showed twice as enhanced RUNX2, ALP, and OCN gene expression of cells within a hydrogel without particles [46,47]. Compared with previous analyses, our results suggest that the encapsulation of TA and SBF biomineral particles is particularly effective for osteogenic differentiation of encapsulated cells because the TMNs are synergistically effective for both osteogenesis and cell viability via ROS scavenging (Fig. 7).

3.7. *In vivo subcutaneous transplantation*

While bone defect models such as critical-sized calvarial defect and femoral bone defect models are more accurate for evaluating bone regeneration [49,50], the primary objective of our study is not bone defect repair but rather the enhancement of cell viability, induction of osteogenic differentiation, and long-term localization of the transplanted cells. Therefore, the subcutaneous model was selected as the appropriate model to achieve these research goals. H&E images after tissue harvesting show that the hydrogels in the G-TMN0 w/cell group rarely degraded, whereas those in the G-TMN2 groups mostly degraded and showed greater infiltration of host cells (Fig. 8a). The incorporation of TMNs within the hydrogel might have decreased the cross-linking density of the hydrogels, promoted host cell infiltration, and accelerated enzymatic matrix degradation. Thus, hydrolysis through matrix metalloproteinase secretion by the infiltrated cells might have contributed to the accelerated hydrogel degradation [51]. The degradation of hydrogels in the presence of collagenase also showed that hydrogels with lower crosslinking density (G-TMN2) degraded faster, and that encapsulated cells accelerated the degradation (Fig. S2). Similar to our results, Lam et al. demonstrated that cells encapsulated within an hyaluronic acid hydrogel promoted degradation when they were in a hydrogel with low crosslinking density [52]. Consistent with our *in vitro* results, the cells within the G-TMN2 hydrogel also showed greater osteogenic differentiation than those within G-TMN0 in the *in vivo* microenvironment (Fig. 8b–d). The von Kossa staining confirmed that the black minerals were found only in the G-TMN2 (Fig. 8b), and only the transplanted cells from G-TMN2 were positive for OCN and OPN, whereas those within both G-TMN0 and G-TMN2 were positive for HNA (Fig. 8c). The RT-qPCR results demonstrate that all osteogenic genes were significantly increased in the hADSCs encapsulated in G-TMN2 compared with those in G-TMN0 (Fig. 8d). Compared with previous results from transplanting osteoconductive hydrogels into *in vivo* subcutaneous tissue, our results demonstrate more dramatic osteoinduction of the cells and ossified tissue in the histological images [53,54].

The cells transplanted in G-TMN2 were aggregated, which was not found in the other groups (Fig. 8b and c). Calcium phosphate mineral particles can bind to serum proteins and biological molecules through ionic interactions and act as cell-binding moieties, which can attract and gather surrounding cells. Enhanced cell-binding affinity of the mineral substrate was also found in previous studies; Xing et al. showed increased adhesion of urine-derived stem cells onto biphasic calcium phosphate ceramics after coating the scaffold with SBF [55]. Bernards et al. demonstrated increased cell adhesion (MC3T3-E1) and serum proteins on a mineralized hydroxyapatite substrate [56]. Furthermore, as shown by HNA staining, the aggregation of cells with particles within G-TMN2 enabled more cells to localize onto the transplanted area compared with cells within G-TMN0, which were dispersed (Fig. 8c). Generally, the long-term localization of cells encapsulated in hydrogels after *in vivo* transplantation has been an unresolved issue because the cells are continuously scattered during degradation of the hydrogel [57]. Taken together, our results suggest that G-TMN2 was effective not only for cell viability via ROS scavenging, but also for osteogenic differentiation of the encapsulated stem cells via calcium phosphate–based osteoinduction, and osteogenesis and long-term delivery of cells were available in the *in vivo* environment.

4. Conclusions

In this study, we designed composite GelMA hydrogels encapsulating stem cell and nanoparticles composed of TA and biominerals. Our investigations of cellular behaviors within the composite hydrogel show that we succeeded in inventing a multifunctional hydrogel that addresses the previously unresolved issues of limited viability due to oxidative stress, limited osteoinduction, and rapid dissociation of cells *in vivo*. First, the G-TMN2 hydrogel (2 mg/mL TMN-2 containing 1.0 mg/mL TA with SBF in GelMA) effectively scavenged both the ROS generated during photo-crosslinking of the GelMA and intracellular ROS, which enhanced the viability and proliferation of the encapsulated cells by mitigating the apoptosis caused by oxidative stress. The hADSCs encapsulated within the G-TMN2 were also strongly induced to differentiate into osteogenic lineages by instructive signals from the biominerals incorporated in the TMNs. Finally, the strong osteogenesis and long-term localization of transplanted cells were demonstrated by *in vivo* analyses after G-TMN2 hydrogels were transplanted into a murine subcutaneous model. Conclusively, our results indicate that our multifunctional composite hydrogel can address the need for a cell-laden photo-cross-linkable hydrogel with marvelous osteogenic induction, and it might be a novel treatment for regenerating bone defects.

CRediT authorship contribution statement

Eunhyung Kim: Writing – review & editing, Writing – original draft, Visualization, Validation, Methodology, Data curation, Conceptualization. **Jinkyu Lee:** Writing – review & editing. **Se-Jeong Kim:** Methodology, Conceptualization. **Eun Mi Kim:** Supervision, Methodology, Conceptualization. **Hayeon Byun:** Conceptualization. **Seung Jae Huh:** Data curation. **Eunjin Lee:** Data curation. **Heungsoo Shin:** Writing – review & editing, Supervision, Funding acquisition, Conceptualization.

Declaration of competing interest

The authors declare that they have no known competing financial interests or personal relationships that could have appeared to influence the work reported in this paper.

Acknowledgments

E.K. and J.L. contributed equally to this work as co-first authors. This work was supported by the National Research Foundation of Korea (NRF) grant funded by the Korean government (MSIT) (grant no. RS-2023-00207983) and Nano & Material Technology Development Program through NRF funded by Ministry of Science and ICT (grant no. RS-2024-00407234).

Appendix A. Supplementary data

Supplementary data to this article can be found online at https://doi.org/10.1016/j.mtbio.2024.101293.

Data availability

Data will be made available on request.

References

[1] J. Ng, K. Spiller, J. Bernhard, G. Vunjak-Novakovic, Biomimetic approaches for bone tissue engineering, Tissue Eng. Part B. Rev. 23 (2017) 480, https://doi.org/10.1089/TEN.TEB.2016.0289.

[2] G.G. Walmsley, R.C. Ransom, E.R. Zielins, T. Leavitt, J.S. Flacco, M.S. Hu, A.S. Lee, M.T. Longaker, D.C. Wan, Stem cells in bone regeneration, Stem Cell Rev. 12 (2016) 524, https://doi.org/10.1007/S12015-016-9665-5.

[3] F. Fiorini, E.A. Prasetyanto, F. Taraballi, L. Pandolfi, F. Monroy, I. López-Montero, E. Tasciotti, L. De Cola, Nanocomposite hydrogels as platform for cells growth, proliferation, and chemotaxis, Small 12 (2016) 4881–4893, https://doi.org/10.1002/SMLL.201601017.

[4] F. Chamieh, A.M. Collignon, B.R. Coyac, J. Lesieur, S. Ribes, J. Sadoine, A. Llorens, A. Nicoletti, D. Letourneur, M.L. Colombier, S.N. Nazhat, P. Bouchard, C. Chaussain, G.Y. Rochefort, Accelerated craniofacial bone regeneration through dense collagen gel scaffolds seeded with dental pulp stem cells, Sci. Rep. 61 (6) (2016) 1–11, https://doi.org/10.1038/srep38814, 2016.

[5] W. Shi, M. Sun, X. Hu, B. Ren, J. Cheng, C. Li, X. Duan, X. Fu, J. Zhang, H. Chen, Y. Ao, W. Shi, X. Hu, B. Ren, J. Cheng, C. Li, X. Duan, X. Fu, J. Zhang, Y. Ao, M. Sun, H. Chen, Structurally and functionally optimized silk-fibroin–gelatin scaffold using 3D printing to repair cartilage injury in vitro and in vivo, Adv. Mater. 29 (2017) 1701089, https://doi.org/10.1002/ADMA.201701089.

[6] M. Zhu, Y. Wang, G. Ferracci, J. Zheng, N.J. Cho, B.H. Lee, Gelatin methacryloyl and its hydrogels with an exceptional degree of controllability and batch-to-batch consistency, Sci. Rep. 91 (9) (2019) 1–13, https://doi.org/10.1038/s41598-019-42186-x, 2019.

[7] R.N. Ghosh, J. Thomas, B.R. Vaidehi, N.G. Devi, A. Janardanan, P.K. Namboothiri, M. Peter, An insight into synthesis, properties and applications of gelatin methacryloyl hydrogel for 3D bioprinting, Mater. Adv. 4 (2023) 5496–5529, https://doi.org/10.1039/D3MA00715D.

[8] N.E. Fedorovich, M.H. Oudshoorn, D. van Geemen, W.E. Hennink, J. Alblas, W.J. A. Dhert, The effect of photopolymerization on stem cells embedded in hydrogels, Biomaterials 30 (2009) 344–353, https://doi.org/10.1016/J.BIOMATERIALS.2008.09.037.

[9] J. Yang, J. Liang, Y. Zhu, M. Hu, L. Deng, W. Cui, X. Xu, Fullerol-hydrogel microfluidic spheres for in situ redox regulation of stem cell fate and refractory bone healing, Bioact. Mater. 6 (2021) 4801–4815, https://doi.org/10.1016/J.BIOACTMAT.2021.05.024.

[10] H.D. Kim, S. Amirthalingam, S.L. Kim, S.S. Lee, J. Rangasamy, N.S. Hwang, Biomimetic materials and fabrication approaches for bone tissue engineering, Adv. Healthc. Mater. 6 (2017) 1700612, https://doi.org/10.1002/ADHM.201700612.

[11] H. Cheng, R. Chabok, X. Guan, A. Chawla, Y. Li, A. Khademhosseini, H.L. Jang, Synergistic interplay between the two major bone minerals, hydroxyapatite and whitlockite nanoparticles, for osteogenic differentiation of mesenchymal stem cells, Acta Biomater. 69 (2018) 342–351, https://doi.org/10.1016/J.ACTBIO.2018.01.016.

[12] M. Rahmati, M. Mozafari, Selective contribution of bioactive glasses to molecular and cellular pathways. https://doi.org/10.1021/acsbiomaterials.8b01078, 2019.

[13] S. Qian, Z. Yan, Y. Xu, H. Tan, Y. Chen, Z. Ling, X. Niu, Carbon nanotubes as electrophysiological building blocks for a bioactive cell scaffold through biological assembly to induce osteogenesis. https://doi.org/10.1039/c9ra00370c, 2019.

[14] N.B. Allen, B. Abar, L. Johnson, J. Burbano, R.M. Danilkowicz, S.B. Adams, 3D-bioprinted GelMA-gelatin-hydroxyapatite osteoblast-laden composite hydrogels for bone tissue engineering, Bioprinting 26 (2022) e00196, https://doi.org/10.1016/J.BPRINT.2022.E00196.

[15] Y. Zuo, X. Liu, D. Wei, J. Sun, W. Xiao, H. Zhao, L. Guo, Q. Wei, H. Fan, X. Zhang, Photo-cross-linkable methacrylated gelatin and hydroxyapatite hybrid hydrogel for modularly engineering biomimetic osteon, ACS Appl. Mater. Interfaces 7 (2015) 10386–10394, https://doi.org/10.1021/acsami.5b01433.

[16] M.T. Tavares, V.M. Gaspar, M.V. Monteiro, J.P. S Farinha, C. Baleizão, J.F. Mano, GelMA/bioactive silica nanocomposite bioinks for stem cell osteogenic differentiation, Biofabrication 13 (2021) 035012, https://doi.org/10.1088/1758-5090/ABDC86.

[17] T. Sun, M. Liu, S. Yao, Y. Ji, L. Shi, K. Tang, Z. Xiong, F. Yang, K. Chen, X. Guo, Guided osteoporotic bone regeneration with composite scaffolds of mineralized ECM/heparin membrane loaded with BMP2-related peptide, Int. J. Nanomed. 13 (2018) 791–804, https://doi.org/10.2147/IJN.S152698.

[18] Y. Guo, Q. Sun, F.-G. Wu, Y. Dai, X. Chen, Y. Guo, Q. Sun, F. Wu, Y. Dai, X. Chen Yong Loo, Polyphenol-containing nanoparticles: synthesis, properties, and therapeutic delivery, Adv. Mater. 33 (2021) 2007356, https://doi.org/10.1002/ADMA.202007356.

[19] E. Torre, Molecular signaling mechanisms behind polyphenol-induced bone anabolism, Phytochem. Rev. 16 (2017) 1183–1226, https://doi.org/10.1007/s11101-017-9529-x.

[20] X. Zhang, Z. Li, P. Yang, G. Duan, X. Liu, Z. Gu, Y. Li, Polyphenol Scaffolds in Tissue Engineering, vol. 8, 2021, p. 145, https://doi.org/10.1039/d0mh01317j.

[21] K. Shin, T. Acri, S. Geary, A.K. Salem, Biomimetic mineralization of biomaterials using simulated body fluids for bone tissue engineering and regenerative medicine, Tissue Eng. Part A. 23 (2017) 1169, https://doi.org/10.1089/TEN.TEA.2016.0556.

[22] J.S. Lee, J.S. Lee, M.S. Lee, S. An, K. Yang, K. Lee, H.S. Yang, H. Lee, S.-W. Cho, Plant flavonoid-mediated multifunctional surface modification chemistry: catechin coating for enhanced osteogenesis of human, Stem Cell. (2017), https://doi.org/10.1021/acs.chemmater.7b00802.

[23] Z. Wei, L. Wang, C. Tang, S. Chen, Z. Wang, Y. Wang, J. Bao, Y. Xie, W. Zhao, B. Su, C. Zhao, Metal-phenolic networks nanoplatform to mimic antioxidant defense system for broad-spectrum radical eliminating and endotoxemia treatment, Adv. Funct. Mater. 30 (2020) 2002234, https://doi.org/10.1002/ADFM.202002234.

[24] Z. Chen, J. Duan, Y. Diao, Y. Chen, X. Liang, H. Li, Y. Miao, Q. Gao, L. Gui, X. Wang, J. Yang, Y. Li, ROS-responsive capsules engineered from EGCG-Zinc networks improve therapeutic angiogenesis in mouse limb ischemia, Bioact. Mater. 6 (2021) 1–11, https://doi.org/10.1016/J.BIOACTMAT.2020.07.013.

[25] S. Lee, Y.-Y. Chang, J. Lee, S. Kumar, M. Perikamana, E.M. Kim, Y.-H. Jung, J.-H. Yun, H. Shin, Surface engineering of titanium alloy using metal-polyphenol network coating with magnesium ions for improved osseointegration, Cite This Biomater. Sci. 8 (2020) 3404, https://doi.org/10.1039/d0bm00566e.

[26] A. Shavandi, A.E.D.A. Bekhit, P. Saeedi, Z. Izadifar, A.A. Bekhit, A. Khademhosseini, Polyphenol uses in biomaterials engineering, Biomaterials 167 (2018) 91–106, https://doi.org/10.1016/J.BIOMATERIALS.2018.03.018.

[27] H. Byun, G.N. Jang, M.H. Hong, J. Yeo, H. Shin, W.J. Kim, H. Shin, Biomimetic anti-inflammatory and osteogenic nanoparticles self-assembled with mineral ions and tannic acid for tissue engineering, Nano Converg 9 (2022), https://doi.org/10.1186/S40580-022-00338-2.

[28] K.-S. Kim, H. Lee, Targeting protein and peptide therapeutics to the heart via tannic acid modification. https://doi.org/10.1038/s41551-018-0227-9, 2018.

[29] N.T.K. Thanh, N. Maclean, S. Mahiddine, Mechanisms of nucleation and growth of nanoparticles in solution, Chem. Rev. 114 (2014) 7610–7630, https://doi.org/10.1021/CR400544S.

[30] C. Sandoval-Acuña, J. Ferreira, H. Speisky, Polyphenols and mitochondria: an update on their increasingly emerging ROS-scavenging independent actions, Arch. Biochem. Biophys. 559 (2014) 75–90, https://doi.org/10.1016/J.ABB.2014.05.017.

[31] C. Pucci, C. Martinelli, D. De Pasquale, M. Battaglini, N. Di Leo, A. Degl'Innocenti, M. Belenli Gümüş, F. Drago, G. Ciofani, Tannic acid-iron complex-based nanoparticles as a novel tool against oxidative stress, ACS Appl. Mater. Interfaces 14 (2022) 15927–15941, https://doi.org/10.1021/ACSAMI.1C24576.

[32] A.P. Dos Santos, Y. Levin, Ion specificity and the theory of stability of colloidal suspensions, Phys. Rev. Lett. 106 (2011) 1–4, https://doi.org/10.1103/PhysRevLett.106.167801.

[33] M.G. Yeo, G.H. Kim, A cell-printing approach for obtaining hASC-laden scaffolds by using a collagen/polyphenol bioink, Biofabrication 9 (2017) 025004, https://doi.org/10.1088/1758-5090/AA6997.

[34] S.-B. Han, J.-K. Kim, G. Lee, D.-H. Kim, S.-B. Han, J.-K. Kim, G.D. Lee, H. Kim, Mechanical properties of materials for stem cell differentiation, Adv. Biosyst. 4 (2020) 2000247, https://doi.org/10.1002/ADBI.202000247.

[35] S.H. Ku, C.B. Park, Human endothelial cell growth on mussel-inspired nanofiber scaffold for vascular tissue engineering, Biomaterials 31 (2010) 9431–9437, https://doi.org/10.1016/J.BIOMATERIALS.2010.08.071.

[36] V. V Belousov, A.F. Fradkov, K.A. Lukyanov, D.B. Staroverov, K.S. Shakhbazov, A. V Terskikh, S. Lukyanov, Genetically encoded fluorescent indicator for intracellular hydrogen peroxide. https://doi.org/10.1038/NMETH866, 2006.

[37] H. Guo, Z. Kuang, J. Zhang, X. Zhao, P. Pu, J. Yan, The preventive effect of Apocynum venetum polyphenols on D-galactose-induced oxidative stress in mice, Exp. Ther. Med. 19 (2020) 557–568, https://doi.org/10.3892/ETM.2019.8261.

[38] K. Yue, G. Trujillo-de Santiago, M.M. Alvarez, A. Tamayol, N. Annabi, A. Khademhosseini, Synthesis, properties, and biomedical applications of gelatin methacryloyl (GelMA) hydrogels, Biomaterials 73 (2015) 254–271, https://doi.org/10.1016/J.BIOMATERIALS.2015.08.045.

[39] Y. Xiong, Y. Xu, F. Zhou, Y. Hu, J. Zhao, Z. Liu, Q. Zhai, S. Qi, Z. Zhang, L. Chen, Bio-functional hydrogel with antibacterial and anti-inflammatory dual properties to combat with burn wound infection, Bioeng. Transl. Med. 8 (2023) e10373, https://doi.org/10.1002/BTM2.10373.

[40] M. Sharifi-Rad, N.V. Anil Kumar, P. Zucca, E.M. Varoni, L. Dini, E. Panzarini, J. Rajkovic, P.V. Tsouh Fokou, E. Azzini, I. Peluso, A. Prakash Mishra, M. Nigam, Y. El Rayess, M. El Beyrouthy, L. Polito, M. Iriti, N. Martins, M. Martorell, A. O. Docea, W.N. Setzer, D. Calina, W.C. Cho, J. Sharifi-Rad, Lifestyle, oxidative stress, and antioxidants: back and forth in the pathophysiology of chronic diseases, Front. Physiol. 11 (2020) 694, https://doi.org/10.3389/fphys.2020.00694.

[41] W.T. Han, T. Jang, S. Chen, L. Shi, H. Chong, H.-D. Jung, J. Song, Improved cell viability for large-scale biofabrication with photo-crosslinkable hydrogel systems through a dual-photoinitiator approach, Cite This Biomater. Sci. 8 (2020) 450, https://doi.org/10.1039/c9bm01347d.

[42] P. Tang, L. Han, P. Li, Z. Jia, K. Wang, H. Zhang, H. Tan, T. Guo, X. Lu, Mussel-Inspired electroactive and antioxidative scaffolds with incorporation of polydopamine-reduced graphene oxide for enhancing skin wound healing, ACS Appl. Mater. Interfaces 11 (2019) 7703–7714, https://doi.org/10.1021/ACSAMI.8B18931.

[43] J. Xiang, C. Wan, R. Guo, D. Guo, Is hydrogen peroxide a suitable apoptosis inducer for all cell types? BioMed Res. Int. 2016 (2016) https://doi.org/10.1155/2016/7343965.

[44] D. Wu, J. Zhou, Y. Shen, C. Lupo, Q. Sun, T. Jin, S.J. Sturla, H. Liang, R. Mezzenga, Highly adhesive Amyloid−Polyphenol hydrogels for, Cell Scaffolding 24 (2022) 480, https://doi.org/10.1021/acs.biomac.2c01311.

[45] M. Singh, H. Sharma, N. Singh, Hydrogen peroxide induces apoptosis in HeLa cells through mitochondrial pathway, Mitochondrion 7 (2007) 367–373, https://doi.org/10.1016/J.MITO.2007.07.003.

[46] H. Wang, B. Hu, H. Li, G. Feng, S. Pan, Z. Chen, B. Li, J. Song, Biomimetic mineralized hydroxyapatite nanofiber-incorporated methacrylated gelatin hydrogel with improved mechanical and osteoinductive performances for bone regeneration, Int. J. Nanomed. 17 (2022) 1511–1529, https://doi.org/10.2147/IJN.S354127.

[47] X. Ding, J. Shi, J. Wei, Y. Li, X. Wu, Y. Zhang, X. Jiang, X. Zhang, H. Lai, A biopolymer hydrogel electrostatically reinforced by amino-functionalized bioactive glass for accelerated bone regeneration, Sci. Adv. 7 (2021), https://doi.org/10.1126/SCIADV.ABJ7857.

[48] X. Gao, Q. Wang, L. Ren, P. Gong, M. He, W. Tian, W. Zhao, Metal-phenolic networks as a novel filler to advance multi-functional immunomodulatory biocomposites, Chem. Eng. J. 426 (2021) 131825, https://doi.org/10.1016/J.CEJ.2021.131825.

[49] J. Yang, C. Deng, M. Shafiq, Z. Li, Q. Zhang, H. Du, S. Li, X. Zhou, C. He, Localized delivery of FTY-720 from 3D printed cell-laden gelatin/silk fibroin composite scaffolds for enhanced vascularized bone regeneration, Smart Mater. Med. 3 (2022) 217–229, https://doi.org/10.1016/J.SMAIM.2022.01.007.

[50] S. Jiang, H. Jing, Y. Zhuang, J. Cui, Z. Fu, D. Li, C. Zhao, U. Liaqat, K. Lin, BMSCs-laden mechanically reinforced bioactive sodium alginate composite hydrogel microspheres for minimally invasive bone repair, Carbohydr. Polym. 332 (2024) 121933, https://doi.org/10.1016/J.CARBPOL.2024.121933.

[51] M.S. Mazzeo, T. Chai, M. Daviran, K.M. Schultz, Characterization of the kinetics and mechanism of degradation of human mesenchymal stem cell-laden poly (ethylene glycol) hydrogels, ACS Appl. Bio Mater. 2 (2019) 81–92, https://doi.org/10.1021/ACSABM.8B00390.

[52] J. Lam, N.F. Truong, T. Segura, Design of cell–matrix interactions in hyaluronic acid hydrogel scaffolds, Acta Biomater. 10 (2014) 1571–1580, https://doi.org/10.1016/J.ACTBIO.2013.07.025.

[53] S. Sharma, D. Sapkota, Y. Xue, Y. Sun, A. Finne-Wistrand, O. Bruland, K. Mustafa, Adenoviral mediated expression of BMP2 by bone marrow stromal cells cultured in 3D copolymer scaffolds enhances bone formation, PLoS One 11 (2016) e0147507, https://doi.org/10.1371/JOURNAL.PONE.0147507.

[54] B. Gaihre, X. Liu, L. Li, A. Lee Miller, E.T. Camilleri, Y. Li, B. Waletzki, L. Lu, Bifunctional hydrogel for potential vascularized bone tissue regeneration, Mater. Sci. Eng. C. 124 (2021) 112075, https://doi.org/10.1016/J.MSEC.2021.112075.

[55] F. Xing, L. Li, J. Sun, G. Liu, X. Duan, J. Chen, M. Liu, Y. Long, Z. Xiang, Surface mineralized biphasic calcium phosphate ceramics loaded with urine-derived stem cells are effective in bone regeneration, J. Orthop. Surg. Res. 14 (2019), https://doi.org/10.1186/S13018-019-1500-7.

[56] M.T. Bernards, C. Qin, S. Jiang, MC3T3-E1 cell adhesion to hydroxyapatite with adsorbed bone sialoprotein, bone osteopontin, and bovine serum albumin, Colloids Surfaces B Biointerfaces 64 (2008) 236–247, https://doi.org/10.1016/J.COLSURFB.2008.01.025.

[57] A.K. Grosskopf, G.A. Roth, A.A.A. Smith, E.C. Gale, H.L. Hernandez, E.A. Appel, Injectable supramolecular polymer–nanoparticle hydrogels enhance human mesenchymal stem cell delivery, Bioeng. Transl. Med. 5 (2020) e10147, https://doi.org/10.1002/BTM2.10147.